



## RESEARCH LETTER

10.1002/2015GL067381

## Key Points:

- Clear frequency-dependent coseismic radiation of this event
- Relation between coseismic radiation and stress drop
- Subducting seamount plays a rupture-barrier role in this region

## Supporting Information:

- Supporting Information S1

## Correspondence to:

H. Yang and H. Yao,  
hyang@cuhk.edu.hk;  
hjyao@ustc.edu.cn

## Citation:

Yin, J., H. Yang, H. Yao, and H. Weng (2016), Coseismic radiation and stress drop during the 2015  $M_w$  8.3 Illapel, Chile megathrust earthquake, *Geophys. Res. Lett.*, 43, doi:10.1002/2015GL067381.

Received 10 DEC 2015

Accepted 22 JAN 2016

Accepted article online 28 JAN 2016

## Coseismic radiation and stress drop during the 2015 $M_w$ 8.3 Illapel, Chile megathrust earthquake

Jiuxun Yin<sup>1,2</sup>, Hongfeng Yang<sup>2</sup>, Huajian Yao<sup>1,3</sup>, and Huihui Weng<sup>2</sup>

<sup>1</sup>Laboratory of Seismology and Physics of Earth's Interior, School of Earth and Space Sciences, University of Science and Technology of China, Hefei, China, <sup>2</sup>Earth System Science Programme, Faculty of Science, Chinese University of Hong Kong, Shatin, Hong Kong, <sup>3</sup>Mengcheng National Geophysical Observatory, Anhui, China

**Abstract** On 16 September 2015, an  $M_w$  8.3 earthquake struck middle Chile due to the subduction of the Nazca plate beneath the South America plate. This earthquake is the consequence of 72 years of strain accumulation in the region since the 1943  $M$  8.3 event. In this study, we apply the compressive sensing method (CS) to invert for the spatiotemporal distribution of the coseismic radiation at different frequencies of this event. The results show clear frequency-dependent feature of earthquake rupture with low-frequency (LF) radiation located in the updip region while high-frequency (HF) radiation concentrated in the downdip region of the megathrust. We also compare the CS results with three coseismic slip models as well as the stress drop distributions inferred from these slip models. The comparison confirms our understanding of coseismic radiation that energy sources are mostly located in the margin of large coseismic slip regions. Furthermore, we find that the LF radiation sources are mainly within the stress-decreasing (releasing) regions while the HF radiation sources are mainly located in the stress-increasing (loading) regions due to rupturing of relatively large asperities nearby (stress decreasing and releasing). These results help to better understand the physics of the rupture process during megathrust earthquakes. Moreover, our results do not show radiation sources south of the epicenter, suggesting that the subducting Juan Fernandez Ridge probably stopped the rupture of this earthquake toward the south.

### 1. Introduction

In the 21st century, there appears to be a global surge of great earthquakes: 19 earthquakes with magnitudes greater than 8 since 2004 [Lay, 2015]. Mitigating losses from these earthquakes demands better understanding of earthquake physics, including the rupture process of great earthquakes. Previous studies have found frequency-dependent coseismic radiation for a few great megathrust earthquakes, including the 2004 Sumatra  $M_w$  9.2, the 2005 Sumatra  $M_w$  8.6, the 2010 Maule  $M_w$  8.8, and the 2011 Tohoku  $M_w$  9.0 earthquakes [e.g., Lay *et al.*, 2012; Yao *et al.*, 2013]. Such phenomena have been attributed to depth-varying frictional/structural properties in subduction zones [Lay *et al.*, 2012]. However, it is still unclear whether the downdip variations of megathrust properties are localized at segments where these great earthquakes occur or are common for the entire subduction zone, due to the resolution limit on the back-projection method and the limited number of megathrust earthquakes. Furthermore, the correspondence of the frequency-dependent coseismic radiation to earthquake rupture physics is of great importance to understand subduction zone earthquakes, yet is still poorly understood.

On 16 September 2015, an  $M_w$  8.3 great earthquake occurred to the west of Illapel, Chile. This earthquake has also generated a tsunami with a maximum wave height of ~4.5 m near Coquimbo and caused great losses in this area. Preliminary slip inversion results indicate that the rupture initiated at ~26 km in depth and propagated northwestward to the shallower part, with a duration of ~130 s (U.S. Geological Survey (USGS): [http://earthquake.usgs.gov/earthquakes/eventpage/us20003k7a#scientific\\_finitefault](http://earthquake.usgs.gov/earthquakes/eventpage/us20003k7a#scientific_finitefault); Earth Observatory of Singapore (EOS): <http://www.earthobservatory.sg/news/september-16-2015-chile-earthquake>). The southern end of the rupture area coincides with the subducting Juan Fernandez Ridge (JFR, Figure 1), which probably prevented the rupture from propagating farther toward the south [Yang *et al.*, 2015]. The rupture region of the 2015 Illapel event locates ~50 km to the north of the 2010  $M_w$  8.8 Maule event, whose rupture area is adjacent to the 1960  $M_w$  9.5 earthquake, the largest earthquake ever recorded in human history (Figure 1). It has been suggested that the postseismic slip of 1960 event has increased the Coulomb stress of 1.3 MPa in the southern

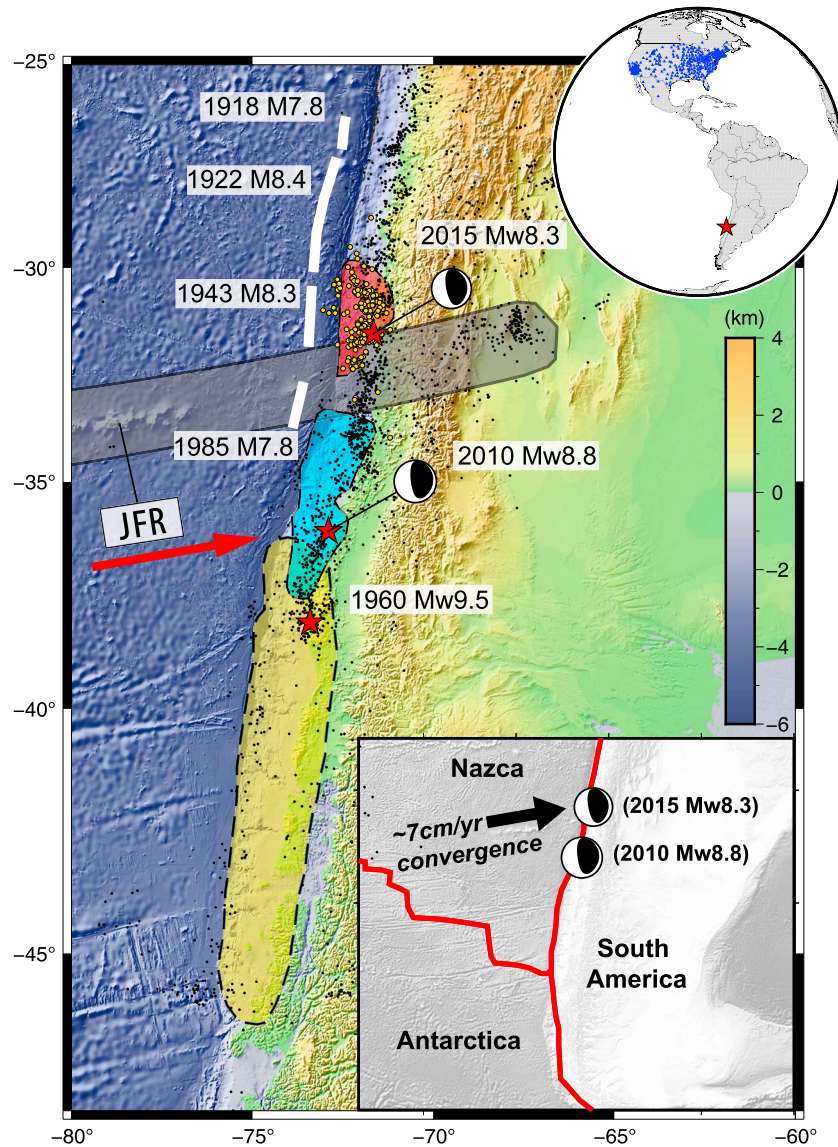


**Figure 1.** Informative map of the southern Chile subduction zone. Black dots are historical earthquakes ( $M > 5$ ) since 1900 and gold circles are aftershocks within 2 days since the 2015 event. Red stars are epicenters of recent three great earthquakes from USGS and two beach balls show focal mechanisms of 2010 and 2015 earthquakes from GCMT (<http://www.globalcmt.org>). White strips represent rupture extents of past great earthquakes from the IRIS website (<http://ds.iris.edu/ds/nodes/dmc/specialevents/2015/09/16/illapel-chile/>). Colored regions show approximate rupture regions of three recent great earthquakes: 1960  $M_w$  9.5 (yellow region) [from *Moreno et al.*, 2009]; 2010  $M_w$  8.8 (blue region) [from *Delouis et al.*, 2010]; 2015  $M_w$  8.3 (red region) (approximately from *Ye et al.* [2015]). Gray shaded region indicates the position and extent of the subducting Juan Fernandez Ridge (JFR) [*Laursen et al.*, 2002]. (top right) The 2015 Chile earthquake epicenter (red star) and the stations (blue triangles) used in this study. (bottom right) Tectonic settings of this region. Bold red lines are the plate boundaries. Black arrow indicates the subducting direction of the Nazca plate relative to the South America plate.

rupture region of the 2010 Maule earthquake, which probably triggered the 2010 Maule event [*Ding and Lin*, 2014]. Such spatial clustering of megathrust earthquakes in Chile poses a classical example of static triggering, similar to the observations along the Sumatra megathrust [*Yang et al.*, 2015].

Although the 2010  $M_w$  8.8 Maule and the 2007  $M_w$  8.0 Peru earthquakes have shown frequency-dependent coseismic radiation [*Wang and Mori*, 2011; *Sufri et al.*, 2012; *Lay et al.*, 2012; *Yao et al.*, 2013], whether other parts of the South America subduction zone share the similar properties remains unknown. The occurrence

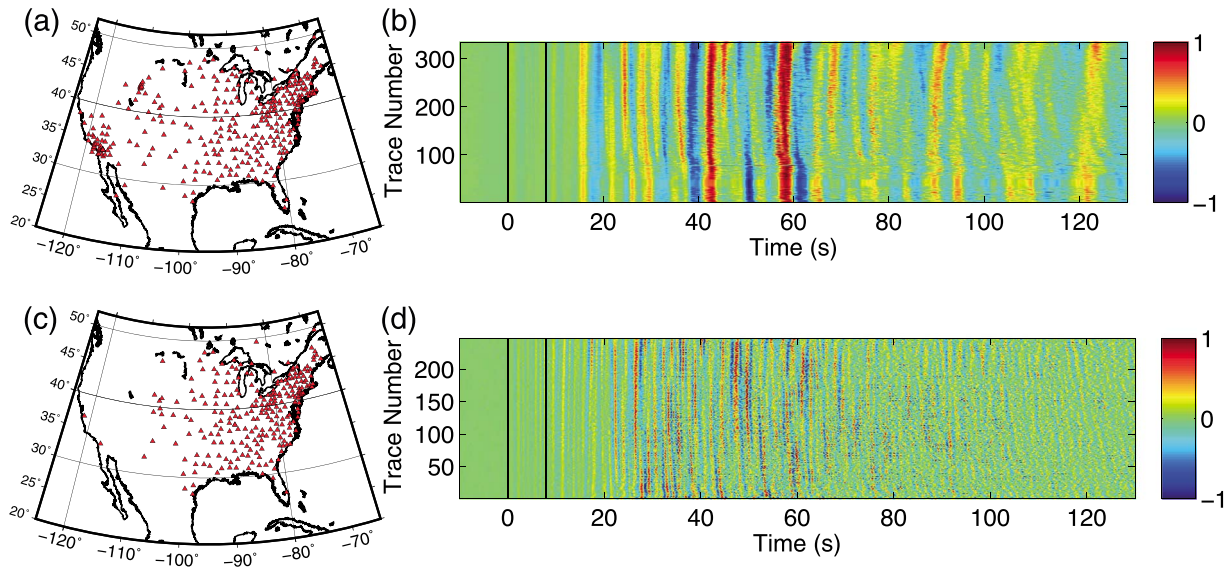


**Figure 2.** (a) Station distribution for low-frequency data. (b) Aligned low-frequency waveform data in the frequency band 0.05–4 Hz. (c) Station distribution for high-frequency data. (d) Aligned high-frequency waveform data in the frequency band 0.5–4 Hz. Within the two black lines (Figures 2b and 2d) are the first 8 s waveforms used to do the cross correlation for waveform alignment.

of the  $M_w$  8.3 Illapel earthquake provides an opportunity to evaluate along-strike variation of properties in this subduction zone. In this work, we investigate the coseismic radiation of the 2015 Chile earthquake in different frequency bands using frequency domain back projection based on an improved compressive sensing (CS) method. We also compute the coseismic stress drop from different finite slip distributions. In order to better understand the observed frequency-dependent phenomenon, we compare our back-projection results with both the coseismic slip and stress drop distribution during this event.

## 2. Method and Data

To study the coseismic radiation during the rupture process of this event, we use the compressive sensing (CS) method, which is a high-resolution sparse inversion method developed from signal processing and applied mathematic community [e.g., Donoho, 2006]. The CS method has been proven very effective to investigate frequency-dependent rupture process of megathrust earthquakes [Yao *et al.*, 2011, 2013]. Compared to the conventional back-projection methods, most of which are based on waveform shifting and stacking and thus often limited by the frequency and geometry of station distribution, CS method is based on L1 norm inversion in the frequency domain and can provide higher resolution, in particular, at lower frequencies [Yao *et al.*, 2013].

The distribution of coseismic radiation during an earthquake can be obtained by solving the following optimization problem:

$$\hat{\mathbf{X}}(\omega) = \operatorname{argmin}(\mathbf{B}(\omega) - \mathbf{A}(\omega)\mathbf{X}(\omega)_1 + r\mathbf{X}(\omega)_1),$$

where  $\mathbf{X}(\omega)$  is the source radiation vector indicating the spatial distribution of coseismic radiation on a projected plane at the focal depth,  $\mathbf{B}(\omega)$  is the observed data vector (spectra) in the frequency domain at the angle frequency of  $\omega$ ,  $\mathbf{A}(\omega)$  is the phase spectrum matrix connecting the source vector and observed spectra [see Yao *et al.*, 2011 for details], and  $r$  is a damping factor balancing the weight of data misfit and model constraints. Based on the L1 norm data misfit and L1 norm model regularization, this CS inversion has very high spatial resolution to resolve sparse sources with resistance against data outliers and can deal with relatively lower frequency waveforms, e.g., within the frequency band of 0.05–0.1 Hz, in which the conventional back-projection (stacking-based) method is difficult to distinguish multiple radiation sources close to each other [Yao *et al.*, 2011]. Here we use the CVX package (<http://cvxr.com>) based on convex optimization and the interior point method [Boyd and Vandenberghe, 2004] to solve the above inverse problem.

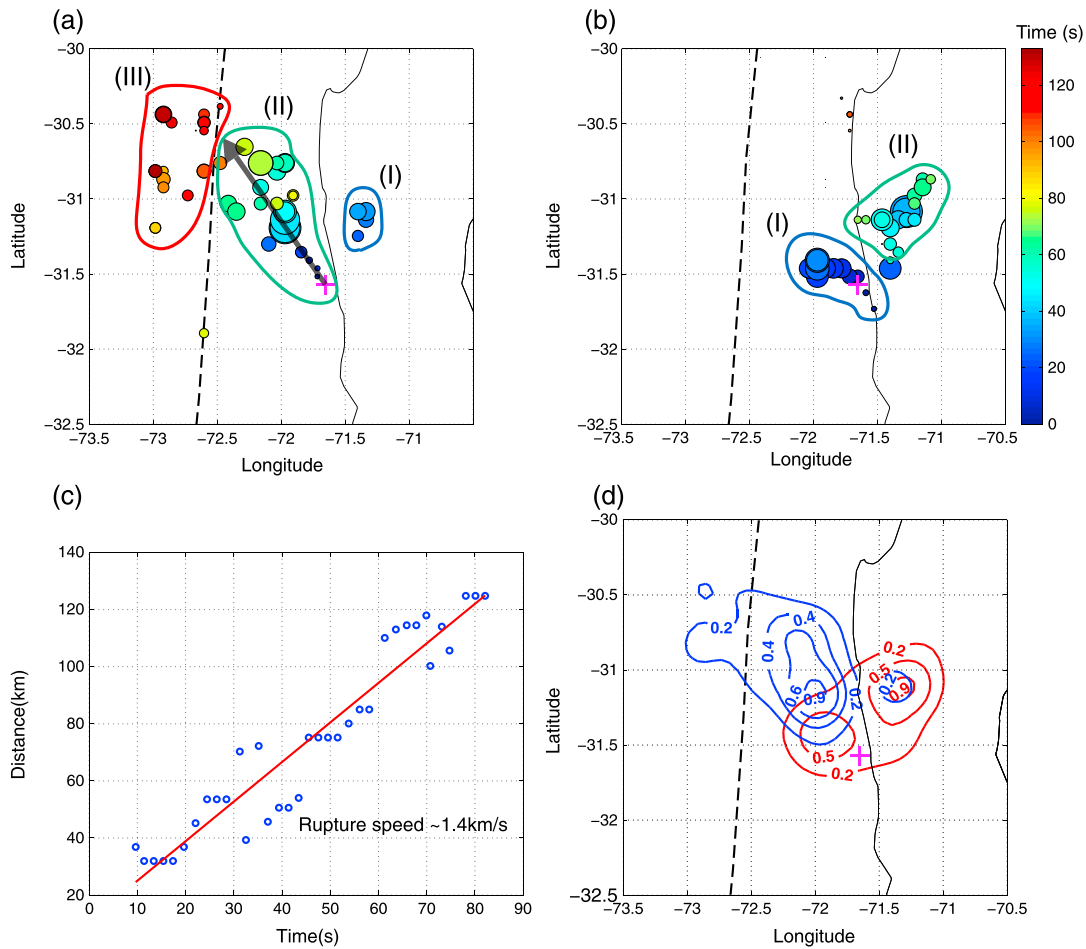


**Figure 3.** (a) Low-frequency (0.05–0.5 Hz) and (b) high-frequency (0.5–1 Hz) CS results of coseismic radiation (circles). Colors represent the time of seismic radiation, and sizes denote the relative energy value. Black arrow indicates the propagation direction of radiation sources. Blue, green, and red curves show the different stages of the coseismic radiation process within: (I) 0–10 s, (II) 10–80 s, and (III) 80–130 s, respectively. (c) Rupture speed estimation for the stage II of low-frequency radiation in Figure 3a. The x axis is the radiation source time (s) and y axis is the projected distance (km) along the propagation direction (black arrow in Figure 3a) from the epicenter. Blue circles are from our results and the red line is the best fitting line with a slope of 1.39 km/s. (d) Scaled total coseismic radiation energy from the CS results for low frequency (blue contours) and high frequency (red contours). Purple cross is the position of the epicenter from USGS.

We obtain teleseismic *P* waves recorded by stations in North America (most in the United States) (Figures 1, 2a, and 2c) within the distance range of 60–85° from the Incorporated Research Institutions for Seismology (IRIS). Because the low-frequency energy (<0.5 Hz) dominates in the data, we filter the data into two different frequency ranges: 0.05–4 Hz and 0.5–4 Hz, and align the waveforms via cross correlation for the first 8 s of the *P* waves, respectively (Figures 2b and 2d). Here we refer low frequency (LF) to 0.05–0.5 Hz and high frequency (HF) to 0.5–1 Hz for our CS results. After preprocessing of the data, we can get the spatiotemporal distribution of the coseismic radiation through a sliding-time window technique (time window length: 14 s for LF and 8 s for HF). All the details about data preprocessing and CS inversion method can be found in our previous work [Yao *et al.*, 2011, 2013]. We also design a synthetic test using waveforms from an  $M_w$  6.5 aftershock near the main shock to test the resolution of our method and check the influences of depth phases on the inversion results (Figure S1 in the supporting information).

To study the rupture process of great earthquakes, coseismic slip and radiation results are often compared with each other. In order to achieve a deeper insight of the physics of seismic radiation, we compute the coseismic shear stress drop during this earthquake using different slip inversion models. Coseismic stress drop describes changes of shear stress on the fault before and after an earthquake and thus is a very important earthquake source parameter that is related to rupture dynamics [Allmann and Shearer, 2009]. In this study we estimate the coseismic stress drop,  $\Delta\tau$ , through a 3-D kinematic modeling process using a finite

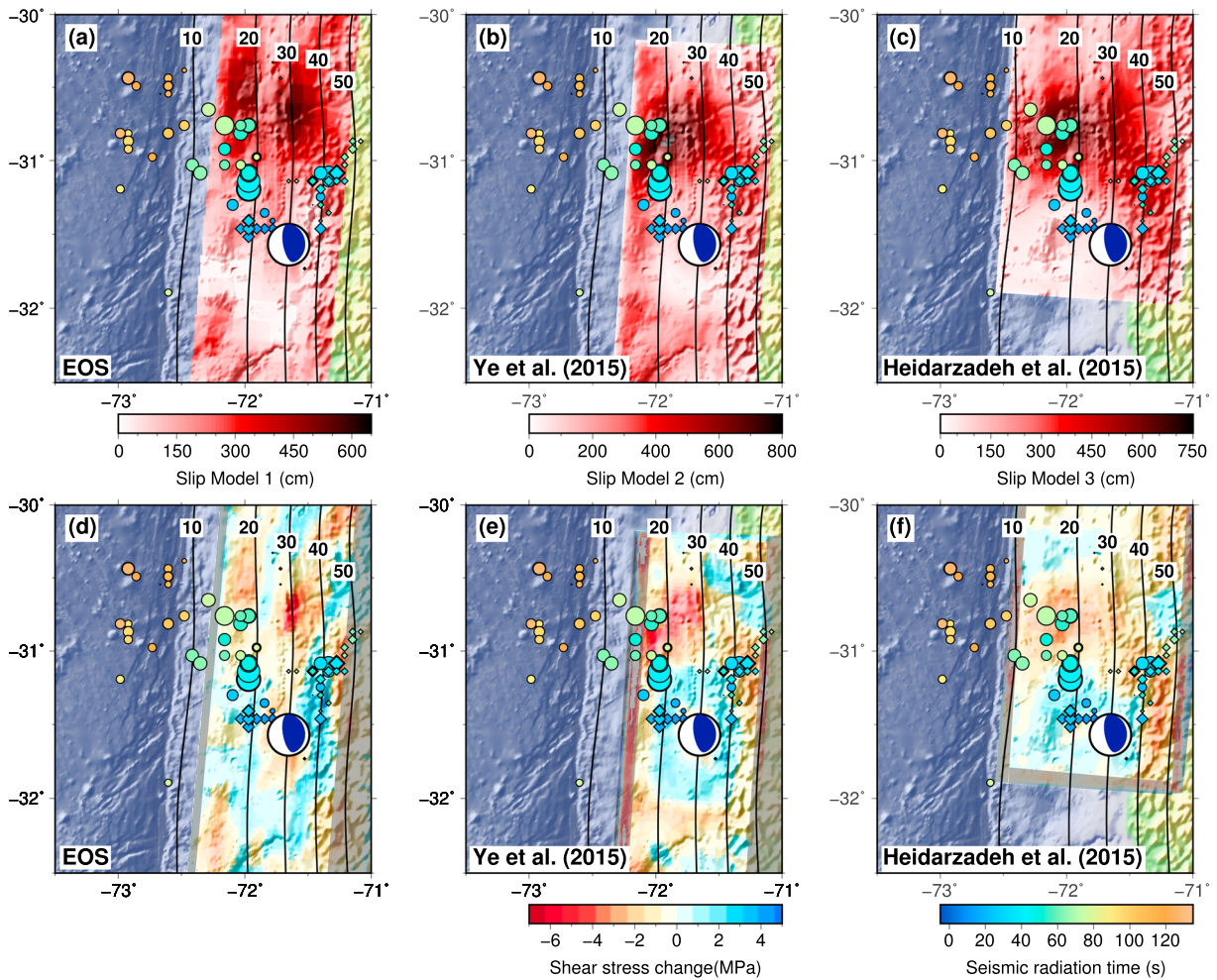


**Figure 4.** Comparison between our CS low-frequency (circles) and high-frequency (diamonds) coseismic radiation results and (a) coseismic slip Model 1 from EOS, (b) coseismic slip Model 2 from *Ye et al.* [2015], (c) coseismic slip Model 3 from *Heidarzadeh et al.* [2015] along with the (d–f) corresponding shear stress changes calculated from these slip models, respectively. Gray marks regions with less reliable solutions due to the lack of slip data or numerical instability near the boundary. Black contours indicate the depth (km) of subducting slab interface from the slab 1.0 model. ([*Hayes et al.*, 2012], data downloaded from USGS website: <http://earthquake.usgs.gov/data/slab/>).

element software, PyLith [*Aagaard et al.*, 2013]. A sufficiently large domain (520 km × 300 km × 100 km) is constructed to avoid the boundary effects. Free slip boundaries (free-slip in the direction normal to the boundary surfaces) are applied on all sides of the domain except for the free surface. The homogeneous materials are set as follows: density = 2700 g/m<sup>3</sup>, Lamé constant  $\lambda = 35.5$  GPa, shear modulus  $\mu = 27.6$  GPa, Poisson’s ratio  $\nu = 0.28$ ,  $V_p = 5.8$  km/s, and  $V_s = 3.2$  km/s. Other parameters such as the geometry of the fault and subfault patches are identical to those in different slip inversion models.

### 3. Results

Our CS results show clear different features between LF and HF coseismic radiation during the 2015  $M_w$  8.3 Chile earthquake (Figure 3). Although the absolute scale of LF radiation is much larger than the HF radiation, the spatial distribution of normalized energy radiation in these two frequency bands indicates clear updip to downdip heterogeneities (Figure 3d): most of the LF radiated energy is located in the updip region (shallower) close to the trench while the HF radiated energy is located in the downdip region (deeper).

Our results also show additional details of the rupture process. For the LF results, the rupture first initiates from the hypocenter and most of the radiation sources propagate unilaterally toward the trench during the first 80 s (Figure 3a, part II). The average rupture speed is ~1.4 km/s within the projected horizontal plane

at the focal depth and  $\sim 1.5$  km/s on the plane considering a  $\sim 20^\circ$  dip of fault geometry. The spatial distribution of this part of radiation corresponds well to the shallower margin of the large slip region in all coseismic slip inversions (Figures 4a–4c). There is also a small portion of radiation located in the downdip region (Figure 3a, part I), and this part of radiation overlaps with the HF radiation (Figure 3b, part II). In the last 40 s (Figure 3a, part III) there are some scattered energy sources radiated from the out-trench regions.

The HF radiation results can be spatiotemporally divided into two different clusters. The first one corresponds to the early stage of the rupture, along with the first 20 s of the LF results. The second cluster (Figure 3b: part II), which has most of the energy in this frequency range ( $>80\%$ ), is originated from the deeper part of the subducting slab interface and starts  $\sim 10$  s later than the part I of the LF results that is located at nearly the same depth. From the HF radiation we have also detected a small part of energy radiation in the north, but the energy is very weak.

Although the slip inversion results show obvious differences (Figures 4a–4c), the shear stress changes computed from these slip models present similar patterns (Figures 4d–4f). Most of the shallow interfaces (10 to 20 km in depth) and regions about 50 km north of the epicenter present clear negative stress changes (stress drop) due to the rupture. The epicenter locates in a region with negative stress change, surrounded by regions with positive stress changes. At  $\sim 40$  km depth northeast of the epicenter, the stress distributions show a relatively complex pattern with both negative and positive stress changes, where complex coseismic radiation patterns with both LF and HF also appear.

## 4. Discussion

### 4.1. Frequency-Dependent Rupture Process

It has been suggested that the LF radiation is associated with large coseismic slip at the shallower portion of the megathrust, whereas the HF radiation corresponds to isolated patches at greater depths [Lay *et al.*, 2012; Yao *et al.*, 2013]. However, we could not clearly find such feature when we compare our results with these slip inversion models (Figures 4a–4c). Slip inversion results present some differences in slip patterns, despite similar technique and fault geometry they have used. For example, In the Slip Model 1 from EOS, the maximum slip region is located at the northern intermediate depth ( $\sim 30$  km) part of the fault with the maximum slip of about 6 m. In stark contrast, the maximum slip occurs at relatively shallower part ( $\sim 20$  km) in Model 2 [Ye *et al.*, 2015] with the largest slip of about 8 m. Our LF radiation results are somewhat consistent with the large slip region of Models 2 and 3 [Heidarzadeh *et al.*, 2015] (Figures 4b and 4c) but are located near the updip margin of the largest slip patch in Model 1 (Figure 4a). In comparison, the HF radiation is roughly following the margin of the largest coseismic slip in Models 1 and 2 (Figures 4a and 4b) but within the deeper rupture region of Model 3 (Figure 4c).

Furthermore, it has been suggested that the downdip seismogenic depths in subduction zones are delineated by either  $350^\circ\text{C}$  isotherm or intersection of continental Moho with the megathrust [Oleskevich *et al.*, 1999]. In the Chile subduction zone near where the 2015 Illapel earthquake occurred, the downdip limit of seismogenic zone has been proposed at  $\sim 40$  km depth due to the presence of serpentinized forearc mantle [Oleskevich *et al.*, 1999]. Our LF coseismic radiation presents the overall features of the unilateral rupture process, initiating at  $\sim 26$  km depth and propagating updip, consistent with the thermal model prediction. Meanwhile, the HF radiation sources are located at depths about 40–50 km, generally consistent with but slightly greater than the suggested downdip limit of seismogenic zone [Oleskevich *et al.*, 1999].

To better understand the correspondence between coseismic radiations at different frequency bands and rupture physics, we then compare our radiation results with the calculated shear stress changes from slip distribution models (Figures 4d–4f). Most of the LF radiation is within the region where shear stress changes are negative (circles in Figures 4d–4f); i.e., stress dropped after being ruptured. This is well expected for relatively smooth ruptures that generally produce large coseismic slip in numerical models of dynamic rupture simulations [e.g., Yang *et al.*, 2013; Weng *et al.*, 2015]. In contrast, the pattern of HF radiation distribution is more complicated: in the shallower part ( $\sim 20$  km) these HF radiation sources in the first 20 s are located in regions with slightly positive stress changes (diamonds at  $\sim 20$  km depth in Figures 4d–4f). These HF energy radiation is probably caused by the abrupt change of rupture speed [Madariaga, 1977] at the margin of a large slip area of this event. Another part of HF radiation is located in the deeper regions with both negative

and positive stress changes. This is consistent with rupturing small isolated asperities at the deeper portion of the megathrust due to the loading (positive stress changes) from nearby larger asperities, which are associated with LF radiation and stress releasing (negative stress changes). Unfortunately, our method and the present slip models do not have sufficient resolution to provide the high-resolution variation of rupture speed or the small-scale detailed stress changes of this 2015 Chile earthquake.

The obvious frequency-dependent radiation observed from our CS results is within our expectation. Similar to the nearby southern 2010  $M_w$  8.8 Maule event [Wang and Mori, 2011; Lay et al., 2012; Yao et al., 2013], most of the LF radiations of this event are located in the shallow part (10–20 km depth) of the subducting slab, corresponding to the conditionally stable to unstable region [Scholz, 1998]. Our results confirm that there is a systematic downdip variation of fault zone properties in the Chile subduction zone, at least along the segments ruptured during the 2010 and 2015 earthquakes. We also locate some out-trench LF radiating sources in the last 40 s (Figure 3a). There are two possible causes of these sources: first, they might be produced by outer-trench events that are triggered during the main shock rupture, as the locations of these sources correspond well to some outer-rise aftershocks. The other possibility is that some of these LF radiation sources are due to multiple-bouncing water phases [e.g., Chu et al., 2011] because our results (Figure 3a, part III) show an approximate propagating pattern of seismic radiation toward the stations, which is similar to the influence of depth phases (see Figure S1a) and consistent with the effect of water phases. However, this part of seismic radiation still needs further investigation.

Both the comparison with coseismic slip and stress drop distribution of our results correspond well to each other, and all of these illustrate clear frequency/depth-dependent properties in the Chile subduction zone. This comparison advances our understanding of coseismic radiation: coseismic radiation is usually located in the margin of coseismic slip region with frequency/depth dependence. Furthermore, the frequency-dependent radiation is closely related to the stress status on the subducting slab: LF radiation tends to be located within the region releasing stress while most of the HF radiations are within the region with positive stress change, that is, from the initiation of rupture or the failure of small scale asperities due to loading. Whether other subduction zone earthquakes have this correspondence needs to be further investigated.

#### 4.2. Implication of Slip Patterns and Subducted Ridges

To estimate the risk of future great earthquakes, the interseismic slip deficit from geodetic measurements in a region is often applied [e.g., McCaffrey et al., 2007; Yang et al., 2015]. For the central Chile subduction zone, previous studies on the interseismic coupling from geodetic observations indicate that this part of subduction zone is highly coupled [Moreno et al., 2010; Métois et al., 2014]. If we assume that the accumulated slip deficit has been reset to 0 since the 1943  $M$  8.3 great earthquake and the plate surface is fully coupled, the total accumulated slip deficit, i.e.,  $7.4 \text{ cm/yr} \times 72 \text{ years} = 5.4 \text{ m}$ , which is smaller than the observed maximum slip (Figures 4a–4c) during this event. Thus, we consider that most of the accumulated strains have already been released, especially at the shallow part of the megathrust. Therefore, the 2015 earthquake has filled in the Comquibo seismic gap since 1943, similar to the case of the neighboring 2010 Maule event [Moreno et al., 2010]. Meanwhile, if we only consider the values of the interseismic slip deficit and coseismic slip, this estimation implies that the accumulated slip during the 1943 event might not be totally released thus leading to larger coseismic slip of this 2015 event.

Although both locking models show the nearly fully coupled fault surface [Moreno et al., 2010; Métois et al., 2014], they do have some significant differences. In the locking model of Moreno et al. [2010] there is an along-strike variation of the locking distributions, corresponding to the EOS slip model. In comparison, the model of Métois et al. [2014] presents a very clear downdip variation similar to the USGS slip model. Furthermore, the locking distributions in the region south of the 2015 epicenter appear in stark contrast between these two models, nearly completely locked [Métois et al., 2014] or almost free sliding [Moreno et al., 2010]. Note that this region is where the JFR is subducting beneath the South America plate for  $\sim 10 \text{ Ma}$  [Larsen et al., 2002]. Although it is unclear how subducting ridges and/or seamounts may influence the plate coupling, the subducting JFR has obvious influences on slab interface and the surface topography/bathymetry.

Our coseismic radiation results do not detect obvious energy from the south of the 2015 epicenter. Thus, we infer that the subducted JFR likely acted as a barrier to inhibit the rupture propagating farther southward [e.g., Yang et al., 2015]. The barrier effects of subducting seafloor roughness have been demonstrated in

numerical simulations given a variety of stress conditions associated with a subducted seamount [Yang *et al.*, 2012, 2013]. In addition, the JFR appears to be associated with a ~50 km gap that spatially separates the rupture regions of the 2010 and 2015 events (Figure 1). Historical records indicate that this segment has been ruptured in the 1985 *M*<sub>w</sub> 7.8 earthquake (Figure 1). Since the neighboring megathrust events likely load this gap, the JFR segment may generate another megathrust earthquake of magnitude ~8 in the future and thus poses significant risk for seismic hazard in central Chile.

## 5. Conclusion

We apply the compressive sensing method to invert for the spatiotemporal distribution of the coseismic radiation of the 2015 *M*<sub>w</sub> 8.3 Illapel earthquake in central Chile and study its rupture process. Our results indicate an overall unilateral rupture process toward the north. We also find obvious frequency-dependent seismic radiation of this event with low-frequency radiation systematically shallower, similar to some previous megathrust events. Specifically, we find that the low-frequency radiation tends to be derived from the area with negative shear stress changes, i.e., stress releasing, while high-frequency radiation sources are mostly generated from the area with shear stress increased by the shallow slip or nearby loading. Our results also imply a probable rupture barrier role of the subducting Juan Fernandez Ridge in this subduction region.

## Acknowledgments

We thank Shengji Wei, Mohammad Heidarzadeh, and Lingling Ye for offering their slip models and U.S. Geological Survey (USGS) for providing the earthquake catalog. All the waveform data are obtained from the Incorporated Research Institutions of Seismology (IRIS), and some of the figures are made from the Generic Mapping Tools (GMT) (<http://gmt.soest.hawaii.edu/>). This study is supported by National Natural Science Foundation of China (41374055), Chinese University of Hong Kong Direct Grant for Research (grant 4053114), Research Grants Council (grant 2191093), and the Fundamental Research Funds for the Central Universities in China (WK2080000053).

## Reference

- Aagaard, B., M. Knepley, and C. Williams (2013), A domain decomposition approach to implementing fault slip in finite-element models of quasi-static and dynamic crustal deformation, *J. Geophys. Res. Solid Earth*, *118*, 3059–3079, doi:10.1002/jgrb.50217.
- Allmann, B. P., and P. M. Shearer (2009), Global variations of stress drop for moderate to large earthquakes, *J. Geophys. Res.*, *114*, B01310, doi:10.1029/2008JB005821.
- Boyd, S., and L. Vandenberghe (2004), *Convex Optimization*, Cambridge Univ. Press, Cambridge, U. K.
- Chu, R., S. Wei, D. V. Helmberger, Z. Zhan, L. Zhu, and H. Kanamori (2011), Initiation of the great *M*<sub>w</sub> 9.0 Tohoku–Oki earthquake, *Earth Planet. Sci. Lett.*, *308*(3), 277–283.
- Delouis, B., J.-M. Nocquet, and M. Vallée (2010), Slip distribution of the February 27, 2010 *M*<sub>w</sub> = 8.8 Maule earthquake, central Chile, from static and high-rate GPS, InSAR, and broadband teleseismic data, *Geophys. Res. Lett.*, *37*, L17305, doi:10.1029/2010GL043899.
- Ding, M., and J. Lin (2014), Post-seismic viscoelastic deformation and stress transfer after the 1960 *M*<sub>w</sub> 9.5 Valdivia, Chile earthquake: Effects on the 2010 *M*<sub>w</sub> 8.8 Maule, Chile earthquake, *Geophys. J. Int.*, *197*(2), 697–704, doi:10.1093/gji/ggu048.
- Donoho, D. L. (2006), Compressed sensing, *IEEE Trans. Inf. Theory*, *52*(4), 1289–1306.
- Hayes, G. P., D. J. Wald, and R. L. Johnson (2012), Slab1.0: A three-dimensional model of global subduction zone geometries, *J. Geophys. Res.*, *117*, B01302, doi:10.1029/2011JB008524.
- Heidarzadeh, M., S. Murotani, K. Satake, T. Ishibe, and A. R. Gusman (2015), Source model of the 16 September 2015 Illapel, Chile *M*<sub>w</sub> 8.4 earthquake based on teleseismic and tsunami data, *Geophys. Res. Lett.*, doi:10.1002/2015GL067297.
- Laursen, J., D. W. Scholl, and R. von Huene (2002), Neotectonic deformation of the central Chile margin: Deepwater forearc basin formation in response to hot spot ridge and seamount subduction, *Tectonics*, *21*(5), 1038, doi:10.1029/2001TC901023.
- Lay, T. (2015), The surge of great earthquakes from 2004 to 2014, *Earth Planet. Sci. Lett.*, *409*, 133–146.
- Lay, T., H. Kanamori, C. J. Ammon, K. D. Koper, A. R. Hutko, L. Ye, H. Yue, and T. M. Rushing (2012), Depth-varying rupture properties of subduction zone megathrust faults, *J. Geophys. Res.*, *117*, B04311, doi:10.1029/2011JB009133.
- Madariaga, R. (1977), High-frequency radiation from crack (stress drop) models of earthquake faulting, *Geophys. J. Int.*, *51*(3), 625–651.
- McCaffrey, R., A. I. Qamar, R. W. King, R. Wells, G. Khazaradze, C. A. Williams, C. W. Stevens, J. J. Vollick, and P. C. Zwick (2007), Fault locking, block rotation and crustal deformation in the Pacific Northwest, *Geophys. J. Int.*, *169*(3), 1315–1340.
- Métis, M., C. Vigny, A. Socquet, A. Delorme, S. Morvan, I. Ortega, and C.-M. Valderas-Bermejo (2014), GPS-derived interseismic coupling on the subduction and seismic hazards in the Atacama region, Chile, *Geophys. J. Int.*, *196*(2), 644–655.
- Moreno, M. S., J. Bolte, J. Klotz, and D. Melnick (2009), Impact of megathrust geometry on inversion of coseismic slip from geodetic data: Application to the 1960 Chile earthquake, *Geophys. Res. Lett.*, *36*, L16310, doi:10.1029/2009GL039276.
- Moreno, M., M. Rosenau, and O. Oncken (2010), 2010 Maule earthquake slip correlates with pre-seismic locking of Andean subduction zone, *Nature*, *467*(7312), 198–202.
- Oleskevich, D. A., R. D. Hyndman, and K. Wang (1999), The updip and downdip limits to great subduction earthquakes: Thermal and structural models of Cascadia, south Alaska, SW Japan, and Chile, *J. Geophys. Res.*, *104*(B7), 14,965–14,991.
- Scholz, C. H. (1998), Earthquakes and friction laws, *Nature*, *391*(6662), 37–42, doi:10.1038/34097.
- Sufri, O., K. D. Koper, and T. Lay (2012), Along-dip seismic radiation segmentation during the 2007 *M*<sub>w</sub> 8.0 Pisco, Peru earthquake, *Geophys. Res. Lett.*, *39*, L08311, doi:10.1029/2012GL051316.
- Wang, D., and J. Mori (2011), Frequency-dependent energy radiation and fault coupling for the 2010 *M*<sub>w</sub> 8.8 Maule, Chile, and 2011 *M*<sub>w</sub> 9.0 Tohoku, Japan, earthquakes, *Geophys. Res. Lett.*, *38*, L22308, doi:10.1029/2011GL049652.
- Weng, H., J. Huang, and H. Yang (2015), Barrier-induced supershear ruptures on a slip-weakening fault, *Geophys. Res. Lett.*, *42*, 4824–4832, doi:10.1002/2015GL064281.
- Yang, H., Y. Liu, and J. Lin (2012), Effects of subducted seamounts on megathrust earthquake nucleation and rupture propagation, *Geophys. Res. Lett.*, *39*, L24302, doi:10.1029/2012GL053892.
- Yang, H., Y. Liu, and J. Lin (2013), Geometrical effects of a subducted seamount on stopping megathrust ruptures, *Geophys. Res. Lett.*, *40*, 2011–2016, doi:10.1002/grl.50509.
- Yang, H., J. Lin, J. Yin, and H. Yao (2015), Tectonic settings of the 2015 *M*<sub>w</sub> 8.3 Coquimbo, Chile earthquake and its implications on megathrust earthquakes [in Chinese], *Chin. Sci. Bull.*, *60*, 3549–3556, doi:10.1360/N972015-01110.

- Yao, H., P. Gerstoft, P. M. Shearer, and C. Mecklenbräuer (2011), Compressive sensing of the Tohoku-Oki  $M_w$  9.0 earthquake: Frequency-dependent rupture modes, *Geophys. Res. Lett.*, *38*, L20310, doi:10.1029/2011GL049223.
- Yao, H., P. M. Shearer, and P. Gerstoft (2013), Compressive sensing of frequency-dependent seismic radiation from subduction zone megathrust ruptures, *Proc. Natl. Acad. Sci. U.S.A.*, *110*(12), 4512–4517.
- Ye, L., T. Lay, H. Kanamori, and K. D. Koper (2015), Rapidly estimated seismic source parameters for the 16 September 2015 Illapel, Chile  $M_w$  8.3 Earthquake, *Pure Appl. Geophys.*, 1–12, doi:10.1007/s00024-015-1202-y.